# Experimental Studies of the Heat Transfer to RBCC Rocket Nozzles for CFD Application to Design Methodologies

**Final Report**
**for**
**NASA Purchase Order H-29688D**

**Robert J. Santoro and Sibtosh Pal**

*Propulsion Engineering Research Center*
*and*
*Department of Mechanical Engineering*
*The Pennsylvania State University*
*University Park, Pennsylvania*

**February, 1999**

PENNSTATE
1855

# Table of Contents

## Abstract

Rocket thrusters for Rocket Based Combined Cycle (RBCC) engines typically operate with hydrogen/oxygen propellants in a very compact space. Packaging considerations lead to designs with either axisymmetric or two-dimensional throat sections. Nozzles tend to be either two- or three-dimensional. Heat transfer characteristics, particularly in the throat, where the peak heat flux occurs, are not well understood. Heat transfer predictions for these small thrusters have been made with one-dimensional analysis such as the Bartz equation or scaling of test data from much larger thrusters. The current work addresses this issue with an experimental program that examines the heat transfer characteristics of a gaseous oxygen ($GO_2$)/gaseous hydrogen ($GH_2$) two-dimensional compact rocket thruster. The experiments involved measuring the axial wall temperature profile in the nozzle region of a water-cooled gaseous oxygen/gaseous hydrogen rocket thruster at a pressure of 3.45 MPa. The wall temperature measurements in the thruster nozzle in concert with Bartz's correlation are utilized in a one-dimensional model to obtain axial profiles of nozzle wall heat flux.

# I Introduction

A steady interest in achieving low cost, reliable access to space drives continued efforts to develop advanced technologies for space transportation systems. A primary element of this goal lies in the development of advanced propulsion systems capable of meeting both performance and mission goals. The Rocket Based Combined Cycle (RBCC) is one promising approach that has received considerable interest throughout the last 30 years. The RBCC design utilizes air-breathing propulsion along with rocket propulsion to take advantage of the ambient oxidizer present in the lower atmosphere. Rocket combustors for RBCC applications are typically compact and "two-dimensional" in geometry. For this geometry, the heat transfer characteristics are not well known due to a lack of experimental investigations. Consequently, heat transfer predictions are based on extrapolating correlations obtained for axisymmetric configurations. The scope of the work presented here was to experimentally investigate the nozzle heat transfer characteristics of a rectangular cross-sectioned compact combustor that was specifically designed for testing the ejector mode of a sector RBCC rig.

The results of experiments conducted on an instrumented rocket nozzle to provide data on the wall temperature achieved under gaseous oxygen ($GO_2$)/gaseous hydrogen ($GH_2$) combustion conditions are reported here. The results are also compared to a simple one-dimensional analysis. The results/analysis have been used by personnel (Mr. P. K. Tucker) at NASA Marshall Space Flight Center to compare to Computational Fluid Dynamics (CFD) heat flux analysis for the same geometry. A joint paper between Penn State and NASA MSFC has been written and submitted for presentation later this year at the 33$^{rd}$ National Heat Transfer Conference hosted by the American Society of Mechanical Engineers (ASME). This paper is attached with this report as an appendix.

# II Experimental Setup

The heat transfer experiments were performed at Penn State's Cryogenic Combustion Laboratory utilizing a multi-section rocket combustor. A schematic of the hardware is shown in Fig. 1., whereas two photographs of the hardware are shown in Fig. 2. The experimental setup includes an injector section, a chamber section, and a thermocouple-instrumented nozzle section. The design of these sections are discussed next.

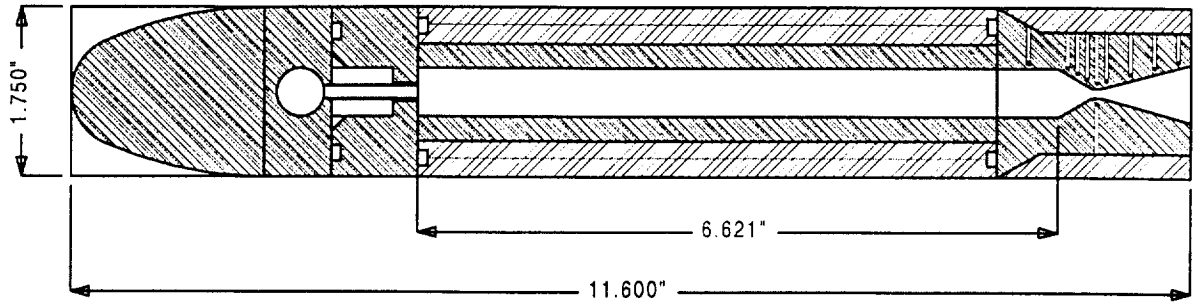


**Fig. 1. Schematic of rocket combustor. The injector has six shear coaxial injector elements arranged linearly. The chamber is 6.6 in. long with a width and height of 3 in. and 0.5 in., respectively. The nozzle throat width and height dimensions are 3 in. and 0.1 in., respectively.**

### 2.1 Rocket Injector

The rocket injector used for the experiments was designed for $GO_2/GH_2$ stoichiometric operation at 500 psia chamber pressure. The injector includes six oxidizer flow centered shear coaxial injector elements that are linearly arranged on the faceplate as seen in Fig. 3. As is evident, the number of elements corresponds to the width to height ratio of the chamber cross section (width = 3 in., height = 0.5 in.) The dimensions of an element are also highlighted in the figure. As seen in the figure, for each element, the thin-walled $GO_2$ post is centered by four 10° angled "posts" that were machined in the hydrogen manifold.

### 2.2 Rocket Chamber

The schematic of the rocket chamber is shown in Fig. 4. The rocket chamber is comprised of an OFHC copper body that is brazed to bottom and top stainless steel plates. The flow cross-section measures 3 in. wide by 0.5 in. high. Water coolant passages are

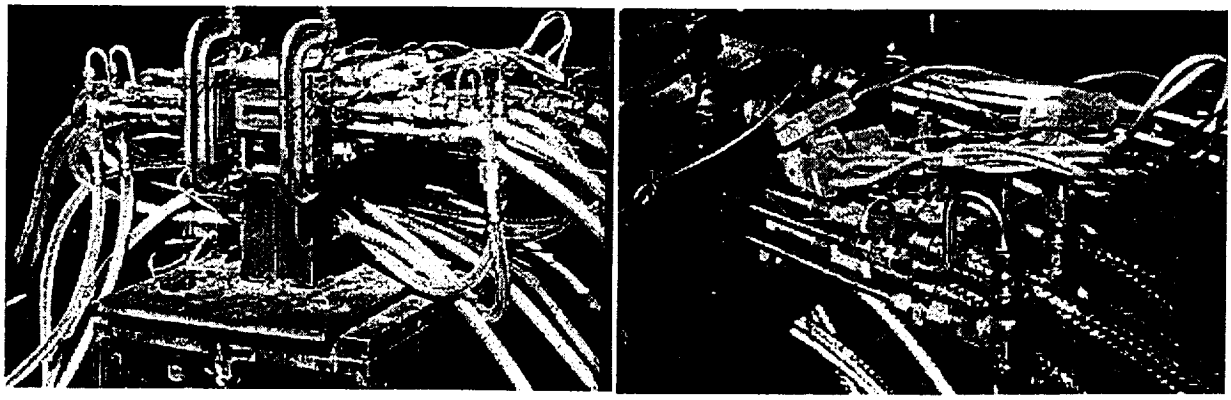

**Fig. 2. Photographs of rocket assembly. Photograph on left shows nozzle exit plane, whereas photograph on right shows a side view of the assembly including the individual thermocouple leads. The thermocouple wires, propellant feed lines, and water coolant lines are also seen.**

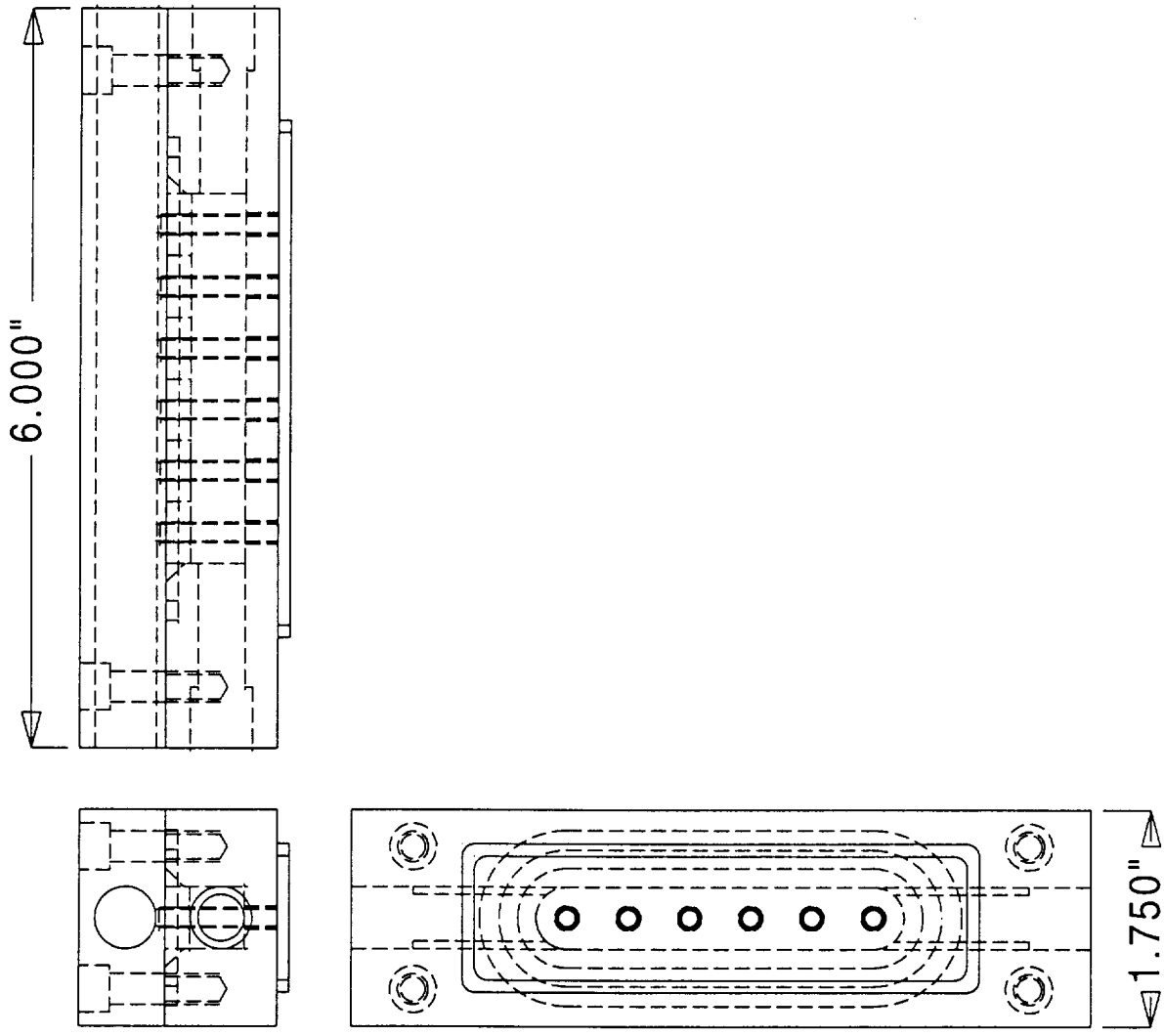


**Fig. 3. Six-element shear coaxial injector assembly. The body is made of OFHC copper, whereas the $GO_2$ posts are made from stainless steel tubing. $GO_2$ post inner and outer diameters are 0.135 in. and 0.165 in., respectively. Outer diameter of $GH_2$ annulus is 0.190 in.**

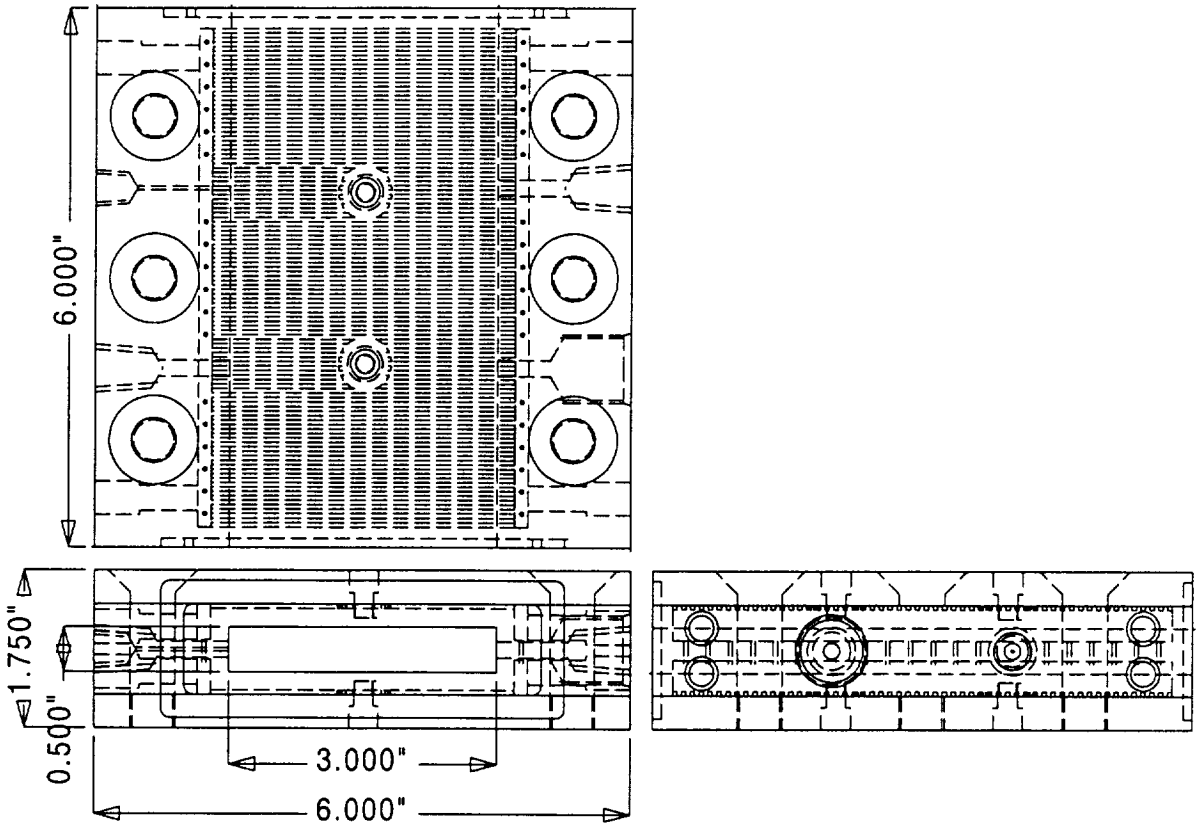


Fig. 4. Rocket chamber section. The chamber is cooled on all four sides. The top and bottom wall are cooled by water flowing through fifty-six 3/64 in. wide by 0.05 in. deep channels, respectively. The bottom of the rectangular water channels is 0.2 in. from the inside chamber walls. Each side wall is cooled by water flowing through eighteen 3/64 in. diameter holes. The rocket chamber body has two inlet and two outlet water manifolds that are linked to the rectangular (top and bottom walls) and circular (side walls) water channels. Each manifold is connected to two 0.375 in. outer diameter (0.28 in. I.D.) tubing.

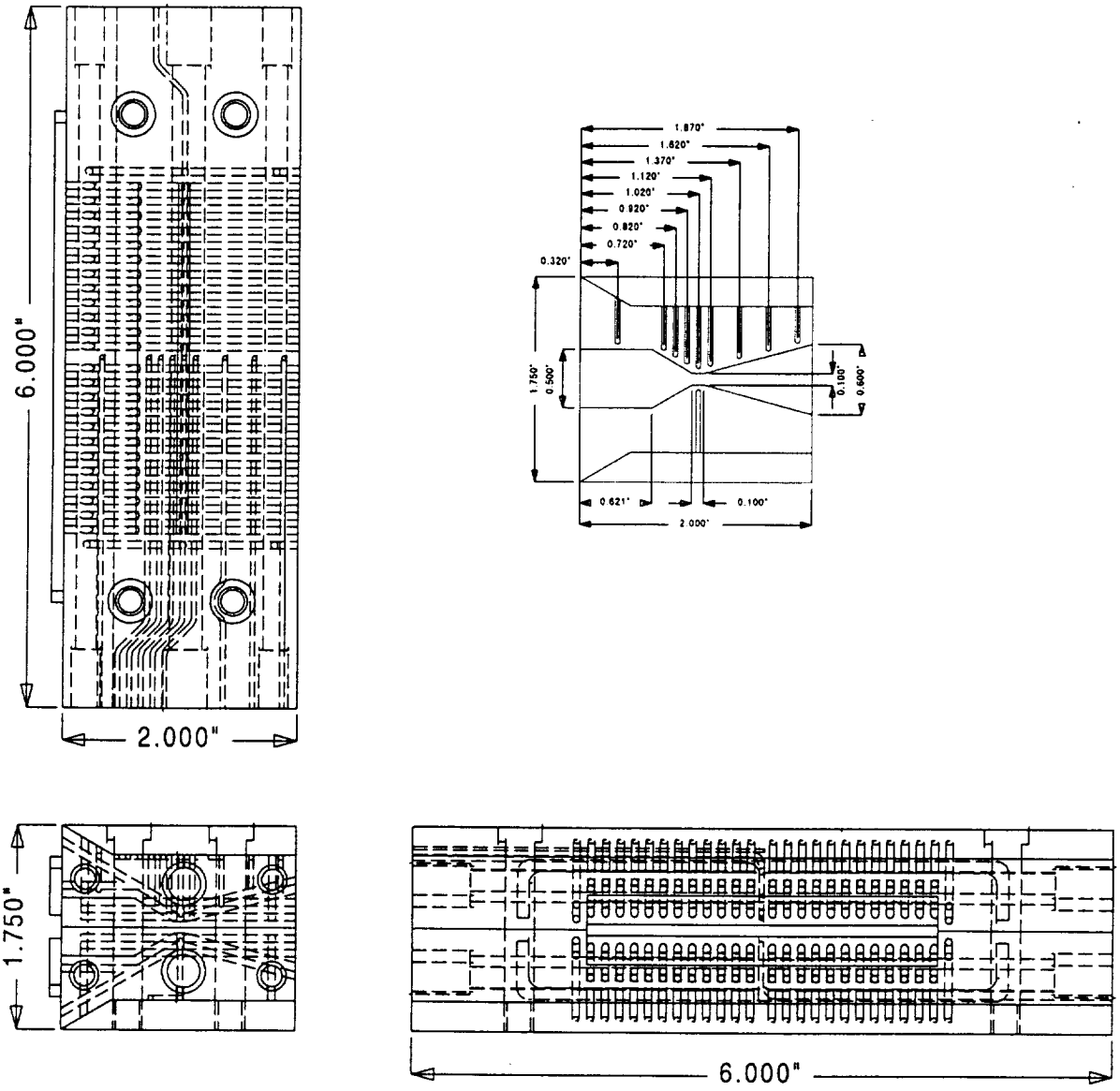


Fig. 5. Instrumented rocket nozzle section. The nozzle is cooled on all four sides. The water cooling passages (1/16 in. diameter holes; 24 each on top and bottom walls and four each on side walls) run parallel to the inside chamber walls. Water enters from the center manifolds, provides impingement cooling to the throat region, bifurcates to cool the converging and diverging sections and then exits through two manifolds. There are four identical independent water circuits (two each on top and bottom) that are separated by a 0.1 in. "land region". The 0.040 in. diameter Type-K thermocouples are silver brazed to the bottom of the thermocouple holes in the "land region" as indicated. All thermocouples are 0.05 in. from the inside hot wall surface.

machined/drilled in the copper body. The top and bottom stainless steel plates brazed to the copper body both seal the water passages and provide structural integrity to the design. Additional support is provided by four stainless steel bolts that attach the top and bottom stainless steel plates. Details regarding the water passages are provided in the figure caption. The chamber is designed to be actively cooled for stoichiometric $GO_2/GH_2$ combustion at pressures up to 500 psia.

### 2.3 Instrumented Rocket Nozzle

A schematic of the instrumented nozzle is shown in Fig. 5. As is evident, the nozzle is heavily water cooled. The descriptions of the cooling circuit and thermocouple locations are provided in the figure. The design includes two OFHC copper sections welded together and supported by two stainless steel plates. The water passages were drilled and closed off by welding. The Type-K thermocouples were silver brazed to the bottom of the holes as indicated in the figure. The thermocouple nomenclature is #1-9 on the top surface in the direction of flow and #10 at the bottom. This process required melting silver material braz to the tip of each thermocouple, filling each thermocouple hole with flux material, positioning each thermocouple such that the tip was at the bottom of the hole and finally, heating the entire assembly beyond the melting temperature of the silver braze material.

The thermocouple mounting required two operations. After the first assembly, all thermocouples were attached correctly; however, the O-ring joint between the nozzle and chamber exhibited a leak. Welding of the seal area was required. During this heating process only thermocouples #3 and #10 remained attached. The second heating process correctly located all the remaining eight thermocouples; however, the results showed that the contact for thermocouples #3 and #10 were compromised during this process. In summary, the measurements indicated that eight (#1, 2, 4, 5, 6, 7, 8 and 9) of the ten thermocouples were operational.

### 2.4 Flow Conditions

Experiments were carried out for the target flow conditions summarized in Table 1. For the experiments, mixture ratios of 4, 6, and 8 and chamber pressures of 200, 300, 400, and 500 psia were tested. Since the rocket hardware was not changed throughout the experiments,

**Table 1. Target Flow Conditions**

| Case # | $GO_2$ Flowrate (lbm/s) | $GH_2$ Flowrate (lbm/s) | O/F | $P_c$ (psia) |
|---|---|---|---|---|
| 1 | 0.1180 | 0.0470 | 4 | 200 |
| 2 | 0.2171 | 0.0362 | 6 | 200 |
| 3 | 0.2433 | 0.0304 | 8 | 200 |
| 4 | 0.2820 | 0.0705 | 4 | 300 |
| 5 | 0.3257 | 0.0543 | 6 | 300 |
| 6 | 0.3650 | 0.0456 | 8 | 300 |
| 7 | 0.3760 | 0.0940 | 4 | 400 |
| 8 | 0.4342 | 0.0724 | 6 | 400 |
| 9 | 0.4866 | 0.0608 | 8 | 400 |
| 10 | 0.4700 | 0.1175 | 4 | 500 |
| 11 | 0.5428 | 0.0905 | 6 | 500 |
| 12 | 0.6083 | 0.0760 | 8 | 500 |

higher chamber pressures were achieved through increased propellant mass flow rates. For each flow condition, two 4 second duration rocket firings were made.

The cooling water flow system was split into two separate lines supplying the rocket chamber and nozzle sections. For each sub-system, the mass flow rate of water was calibrated for upstream manifold pressure. For each firing, inlet manifold pressure as well as inlet and exit water temperature were recorded.

## III Experimental Results

For each target flow condition in Table 1, the actual rocket operating flow condtions were recorded. The thermocouple measurements were recorded at 200 Hz for a total of 10 seconds which included time before, during and after the firing sequence. All averaged results pertaining to each firing are summarized in Table 2. Note that all numbers presented in the spreadsheet are averaged over the final 1.5 second duration of each firing. The results are tabulated in case number order (as per Table 1).

The temperature versus time plot for all eight operational thermocouples are presented in Fig. 6 for Case 12, Table 1 corresponding to the O/F=8, chamber pressure of 500 psia case. The corresponding inlet and outlet measured water temperatures are plotted versus time in Fig. 7. The measurements show that steady state conditions are achieved within the first one second of the firing. The nozzle temperature measurements show that the temperature increases in the

converging section, maximizes at the throat and then decreases in the diverging section. Inspection of results for the other rocket operating conditions yields the same qualitative conclusions.

In the following section, a one-dimensional analysis is presented for the O/F=8 chamber pressure of 500 psia case.

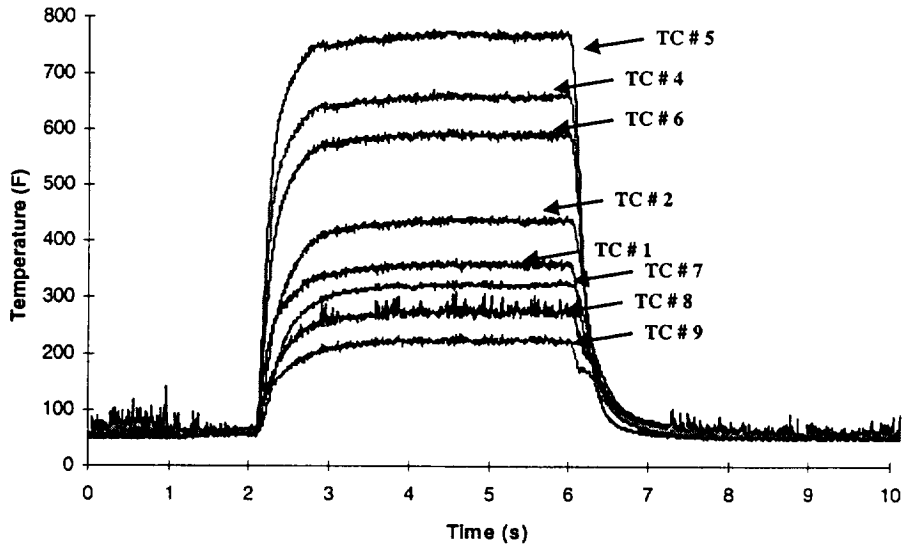


**Fig. 6. Temperature versus time for rocket nozzle. O/F=8, $P_c$= 500 psia. Note that all thermocouples achieve steady state temperature within one second. For thermocouple locations, refer to Fig. 5.**

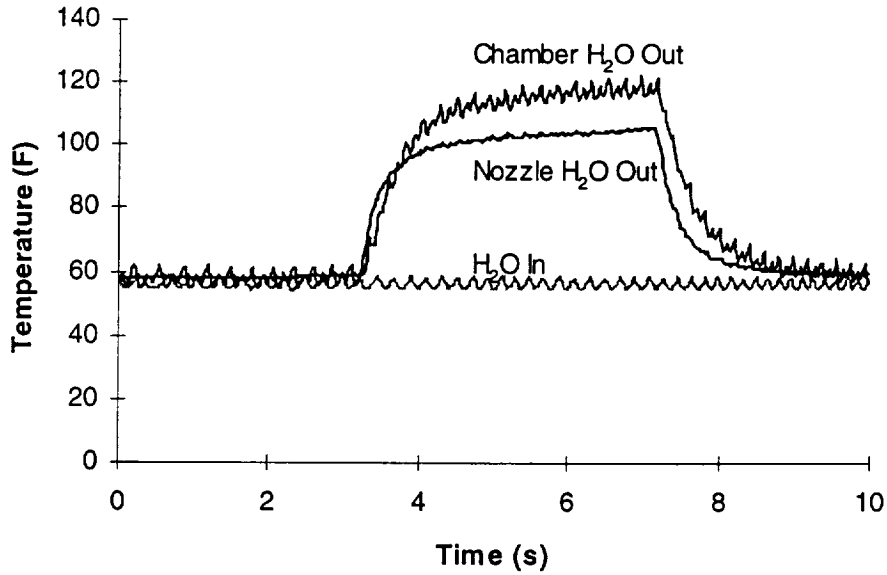


**Fig. 7. Inlet and outlet water flow temperatures versus time for rocket nozzle. . O/F=8, $P_c$= 500 psia. (Note that "zero" time for this graph is linearly translated from that of Fig. 6.**

## Table 2. Summary of Experimental Measurements (Flow Conditions)

| | | mdot (lbm/sec) | | | | | | |
|---|---|---|---|---|---|---|---|---|
| **Case #** | **Run #** | Fuel | Oxidizer | Total | P Ch. (psia) | Target P. Ch. | O/F | Target O/F |
| *1* | *11* | 0.05 | 0.20 | 0.25 | 203.1 | 200 | 4.11 | 4 |
| *1* | *13* | 0.05 | 0.20 | 0.25 | 206.3 | 200 | 3.95 | 4 |
| *1* | *15* | 0.05 | 0.20 | 0.25 | 204.6 | 200 | 3.99 | 4 |
| *1* | *37* | 0.05 | 0.20 | 0.25 | 205.7 | 200 | 4.20 | 4 |
| *2* | *17* | 0.04 | 0.23 | 0.26 | 204.4 | 200 | 5.94 | 6 |
| *2* | *18* | 0.04 | 0.23 | 0.26 | 202.4 | 200 | 6.09 | 6 |
| *2* | *38* | 0.04 | 0.22 | 0.26 | 197.4 | 200 | 6.04 | 6 |
| *3* | *19* | 0.03 | 0.25 | 0.28 | 203.0 | 200 | 7.87 | 8 |
| *3* | *21* | 0.03 | 0.26 | 0.29 | 206.9 | 200 | 7.92 | 8 |
| *3* | *39* | 0.03 | 0.26 | 0.29 | 203.2 | 200 | 8.04 | 8 |
| *4* | *40* | 0.07 | 0.30 | 0.37 | 305.4 | 300 | 4.31 | 4 |
| *4* | *41* | 0.07 | 0.30 | 0.37 | 307.6 | 300 | 4.18 | 4 |
| *5* | *33* | 0.06 | 0.33 | 0.39 | 302.0 | 300 | 5.96 | 6 |
| *5* | *35* | 0.06 | 0.33 | 0.39 | 299.8 | 300 | 6.02 | 6 |
| *6* | *22* | 0.05 | 0.37 | 0.42 | 301.0 | 300 | 7.86 | 8 |
| *6* | *31* | 0.05 | 0.37 | 0.42 | 303.1 | 300 | 7.81 | 8 |
| *6* | *36* | 0.05 | 0.37 | 0.42 | 300.3 | 300 | 7.95 | 8 |
| *7* | *47* | 0.10 | 0.40 | 0.50 | 406.5 | 400 | 4.13 | 4 |
| *7* | *49* | 0.10 | 0.41 | 0.51 | 413.5 | 400 | 4.24 | 4 |
| *8* | *45* | 0.07 | 0.45 | 0.53 | 403.6 | 400 | 6.04 | 6 |
| *8* | *46* | 0.08 | 0.45 | 0.53 | 405.6 | 400 | 6.02 | 6 |
| *9* | *42* | 0.06 | 0.51 | 0.57 | 407.0 | 400 | 8.03 | 8 |
| *9* | *43* | 0.06 | 0.51 | 0.57 | 403.5 | 400 | 8.10 | 8 |
| **10** | **52** | n/a | n/a | n/a | n/a | 500 | n/a | 4 |
| *11* | *53* | 0.09 | 0.56 | 0.65 | 481.7 | 500 | 6.02 | 6 |
| *12* | *50* | 0.08 | 0.63 | 0.70 | 487.3 | 500 | 8.01 | 8 |
| *12* | *51* | 0.08 | 0.63 | 0.71 | 484.0 | 500 | 8.14 | 8 |

**Table 2. Summary of Experimental Measurements (*continued*)**
**(Nozzle Thermocouple Measurements)**

| | | Nozzle TCs | | | | | | | |
|---|---|---|---|---|---|---|---|---|---|
| **Case #** | **Run #** | TC1 Deg. F | TC2 Deg. F | TC4 Deg. F | TC5 Deg. F | TC6 Deg. F | TC7 Deg. F | TC8 Deg. F | TC9 Deg. F |
| *1* | *11* | 223.8 | 223.0 | 273.8 | 319.5 | 257.4 | 158.7 | 144.8 | 118.0 |
| *1* | *13* | 223.5 | 223.8 | 276.4 | 321.3 | 257.0 | 158.6 | 147.5 | 118.2 |
| *1* | *15* | 224.2 | 224.3 | 276.1 | 321.2 | 258.7 | 159.6 | 147.7 | 118.8 |
| *1* | *37* | 230.9 | 225.4 | 286.9 | 330.2 | 266.7 | 164.5 | 153.4 | 121.6 |
| *2* | *17* | 249.0 | 253.5 | 320.0 | 374.0 | 290.6 | 170.3 | 149.8 | 111.8 |
| *2* | *18* | 248.1 | 251.1 | 316.6 | 370.7 | 288.3 | 169.8 | 150.2 | 111.2 |
| *2* | *38* | 249.2 | 245.0 | 312.2 | 361.9 | 285.2 | 171.4 | 158.7 | 113.9 |
| *3* | *19* | 246.3 | 250.8 | 309.4 | 360.3 | 277.0 | 165.4 | 148.2 | 108.0 |
| *3* | *21* | 247.2 | 251.4 | 311.4 | 363.8 | 279.6 | 165.8 | 149.9 | 108.8 |
| *3* | *39* | 247.0 | 247.3 | 309.8 | 354.3 | 274.4 | 166.5 | 158.2 | 111.6 |
| *4* | *40* | 277.9 | 289.9 | 397.3 | 460.0 | 365.3 | 217.4 | 198.1 | 154.4 |
| *4* | *41* | 276.5 | 287.9 | 394.5 | 455.2 | 362.5 | 216.1 | 198.4 | 154.5 |
| *5* | *33* | 294.2 | 316.3 | 442.1 | 512.7 | 395.2 | 223.8 | 191.6 | 149.2 |
| *5* | *35* | 293.0 | 313.8 | 439.7 | 511.5 | 393.4 | 221.9 | 190.0 | 147.9 |
| *6* | *22* | 394.5 | 394.5 | 394.5 | 394.5 | 394.5 | 394.5 | 394.5 | 394.5 |
| *6* | *31* | 293.6 | 321.8 | 434.3 | 499.2 | 381.5 | 214.9 | 186.9 | 148.5 |
| *6* | *36* | 291.3 | 318.5 | 430.3 | 492.6 | 377.5 | 213.0 | 185.6 | 147.4 |
| *7* | *47* | 310.7 | 340.3 | 486.1 | 553.3 | 437.3 | 258.2 | 225.4 | 180.2 |
| *7* | *49* | 313.2 | 343.7 | 492.2 | 558.5 | 442.6 | 260.4 | 228.7 | 183.5 |
| *8* | *45* | 339.0 | 392.0 | 560.9 | 653.7 | 503.7 | 283.5 | 250.6 | 197.8 |
| *8* | *46* | 341.0 | 395.3 | 566.5 | 660.8 | 508.8 | 286.7 | 250.5 | 198.9 |
| *9* | *42* | 336.3 | 387.4 | 542.0 | 636.2 | 490.2 | 272.4 | 237.5 | 188.4 |
| *9* | *43* | 335.4 | 385.7 | 541.0 | 633.6 | 488.1 | 273.0 | 241.2 | 189.7 |
| **10** | **52** | 345.6 | 390.7 | 579.1 | 661.1 | 518.9 | 298.5 | 258.9 | 210.2 |
| *11* | *53* | 360.4 | 423.1 | 638.0 | 735.0 | 570.3 | 320.7 | 277.5 | 223.8 |
| *12* | *50* | 362.9 | 433.8 | 652.2 | 763.4 | 588.9 | 323.0 | 276.3 | 223.8 |
| *12* | *51* | 363.3 | 435.3 | 657.7 | 767.6 | 589.5 | 320.8 | 275.3 | 224.0 |

## Table 2. Summary of Experimental Measurements (*continued*) (Nozzle Water Flow)

| | | TEMP | both on top..... | | | | Flow Rates (lbm/s) | |
|---|---|---|---|---|---|---|---|---|
| **Case #** | **Run #** | $H_2O$ In | Ch $H_2O$ out | Nozzle $H_2O$ Out Average | Nozzle $H_2O$ Out 1 | Nozzle $H_2O$ Out 2 | mdot nozzle | mdot Ch. |
| *1* | *11* | 56.36 | n/a | 77.25 | 73.12 | 81.38 | 5.16 | 7.30 |
| *1* | *13* | 56.46 | n/a | 77.63 | 73.5 | 81.76 | 5.21 | 7.40 |
| *1* | *15* | 56.19 | n/a | 77.31 | 73.173 | 81.45 | 5.18 | 7.39 |
| *1* | *37* | 56.41 | 93.34 | 79.155 | 74.73 | 83.58 | 5.13 | 7.30 |
| *2* | *17* | 56.21 | n/a | 78.41 | 74.26 | 82.56 | 5.18 | 7.38 |
| *2* | *18* | 56.18 | n/a | 77.87 | 73.79 | 81.95 | 5.18 | 7.38 |
| *2* | *38* | 56.32 | 88.85 | 78.22 | 74.05 | 82.39 | 5.11 | 7.25 |
| *3* | *19* | 56.31 | n/a | 76.45 | 73.08 | 79.82 | 5.19 | 7.38 |
| *3* | *21* | 56.3 | n/a | 77.25 | 73.31 | 80.19 | 5.15 | 7.36 |
| *3* | *39* | 56.18 | 85.13 | 76.655 | 73.21 | 80.1 | 5.20 | 7.38 |
| *4* | *40* | 56.33 | 106.14 | 87.755 | 81.92 | 93.59 | 5.21 | 7.38 |
| *4* | *41* | 56.33 | 106.88 | 88.015 | 82.06 | 93.97 | 5.21 | 7.39 |
| *5* | *33* | 56.59 | n/a | 87.16 | 82.07 | 92.25 | 5.15 | 7.32 |
| *5* | *35* | 56.45 | 99.96 | 87.135 | 81.98 | 92.24 | 5.14 | 7.30 |
| *6* | *22* | 56.1 | n/a | 84.005 | 79.65 | 88.36 | 5.16 | 7.35 |
| *6* | *31* | 56.74 | n/a | 84.735 | 80.48 | 88.99 | 5.15 | 7.33 |
| *6* | *36* | 56.35 | 96.04 | 84.485 | 80.26 | 88.71 | 5.13 | 7.30 |
| *7* | *47* | 56.31 | 120.95 | 98.355 | 89.78 | 106.93 | 5.17 | 7.34 |
| *7* | *49* | 56.12 | 121.8 | 99.35 | 90.24 | 108.46 | 5.19 | 7.36 |
| *8* | *45* | 56.15 | 112.497 | 96.845 | 90.12 | 103.57 | 5.19 | 7.36 |
| *8* | *46* | 56.36 | 113.44 | 97.655 | 90.73 | 104.58 | 5.19 | 7.37 |
| *9* | *42* | 56.43 | 106.86 | 93.88 | 88.58 | 99.18 | 5.20 | 7.38 |
| *9* | *43* | 56.29 | 106.29 | 93.7 | 88.41 | 98.99 | 5.19 | 7.36 |
| **10** | **52** | n/a | n/a | n/a | n/a | n/a | n/a | n/a |
| *11* | *53* | 56.4 | 122.57 | 106.995 | 97.89 | 116.1 | 5.13 | 7.27 |
| *12* | *50* | 55.98 | 115.78 | 102.71 | 95.68 | 109.74 | 5.17 | 7.33 |
| *12* | *51* | 56.45 | 117.17 | 104.44 | 96.88 | 112 | 5.17 | 7.33 |

# IV One-Dimensional Analysis

A simple one-dimensional analysis for the O/F=8, $P_c$=500 psia case is presented in this section. This case is chosen since the nozzle geometry was optimized for isentropic expansion under these conditions. The one-dimensional assumption asserts that at any axial location within the nozzle, all temperatures are constant. While this assumption may not be truly accurate, deviation from one-dimensionality can not be accounted for with the current measurements.

The analysis presented here is based on simple energy balance. Under steady state conditions, the bulk energy increase in the cooling water is equal to the heat transferred to the nozzle wall from the hot gasses. There is no ambiguity in the measurement of the change in temperature of the cooling fluid. The total heat transferred from the hot gas to the chamber wall is calculated by integrating along the nozzle flow path. For the integration, Bartz's Correlation [1] is used for obtaining the convective heat transfer coefficient.

$$h_g = \left[\frac{0.026}{(D^*)^{0.2}}\left(\frac{\mu^{0.2}}{\mathrm{Pr}^{0.6}}C_p\right)_0\left(\frac{P_0}{c^*}\right)^{0.8}\left(\frac{D^*}{r_c}\right)^{0.1}\right]\left(\frac{A^*}{A}\right)^{0.9}\sigma \tag{1}$$

where

$(\ )_0$ represents stagnation conditions

$h_g$ = convective heat transfer coefficient

$\mu$ = dynamic viscosity

$C_p$ = specific heat

Pr = Prandtl number

$c^*$ = characteristic velocity

$D^*$ = throat diameter, taken here as hydraulic diameter

$r_c$ = throat radius of curvature, taken as 0.1 in. here

$$\sigma = \frac{1}{\left[\frac{1}{2}\frac{T_{wg}}{T_{0g}}\left(1+\frac{\gamma-1}{2}M^2\right)+\frac{1}{2}\right]^{0.8-.2\omega}\left(1+\frac{\gamma-1}{2}M^2\right)^{0.2\omega}} \tag{2}$$

$M$ = local Mach number

$T_{wg}$ = hot side wall temperature

$T_{0g}$ = hot gas stagnation temperature

$\omega$ = 0.6 for diatomic gasses (assumed to be correct here)

For the above equation the quantity in the square brackets is a constant throughout the converging-diverging section of the nozzle.

Since the nozzle thermocouples measure the metal temperature 0.05 in. from the hot wall surface, the following equation is used to calculate the temperature at the hot wall surface:

$$-k\frac{T_{thermocouple}-T_{wg}}{\Delta y}=h_g(T_{0g}-T_{wg}) \qquad (3)$$

The use of this equation is based on the assumption that conduction occurs only normal to the boundaries, i.e. axial conduction in the metal is not considered.

The above three coupled equations were numerically integrated to obtain the heat transfer for the O/F=8, $P_c$=500 psia case. Properties were obtained using CEA [2]. For the integration, the nozzle was divided into four sections, viz. straight section, converging section, throat section, and the diverging section. For the constant area sections, constancy was assumed. Axial profiles of key parameters are plotted in Fig. 8. The axial plots for hot gas wall temperature, heat transfer coefficient, and heat flux show the expected trends. The energy balances show good agreement between the integrated approach and the bulk energy increase of the coolant water flow.

## V Summary

The good agreement in energy balance for the analysis with the assumptions of one-dimensionality and the Bartz's correlation for the prediction of the heat transfer coefficient was encouraging in terms of confidence in the use of Bartz's equation for small scale rectangular rocket thrusters. Additionally, the measured axial profiles of the nozzle wall temperatures for a range of flow conditions can be used for anchoring/evaluating CFD approaches for predicting nozzle heat flux levels. Discussions on complementary CFD efforts carried out by Mr. P. K. Tucker of NASA MSFC can be found in the paper attached as an appendix.

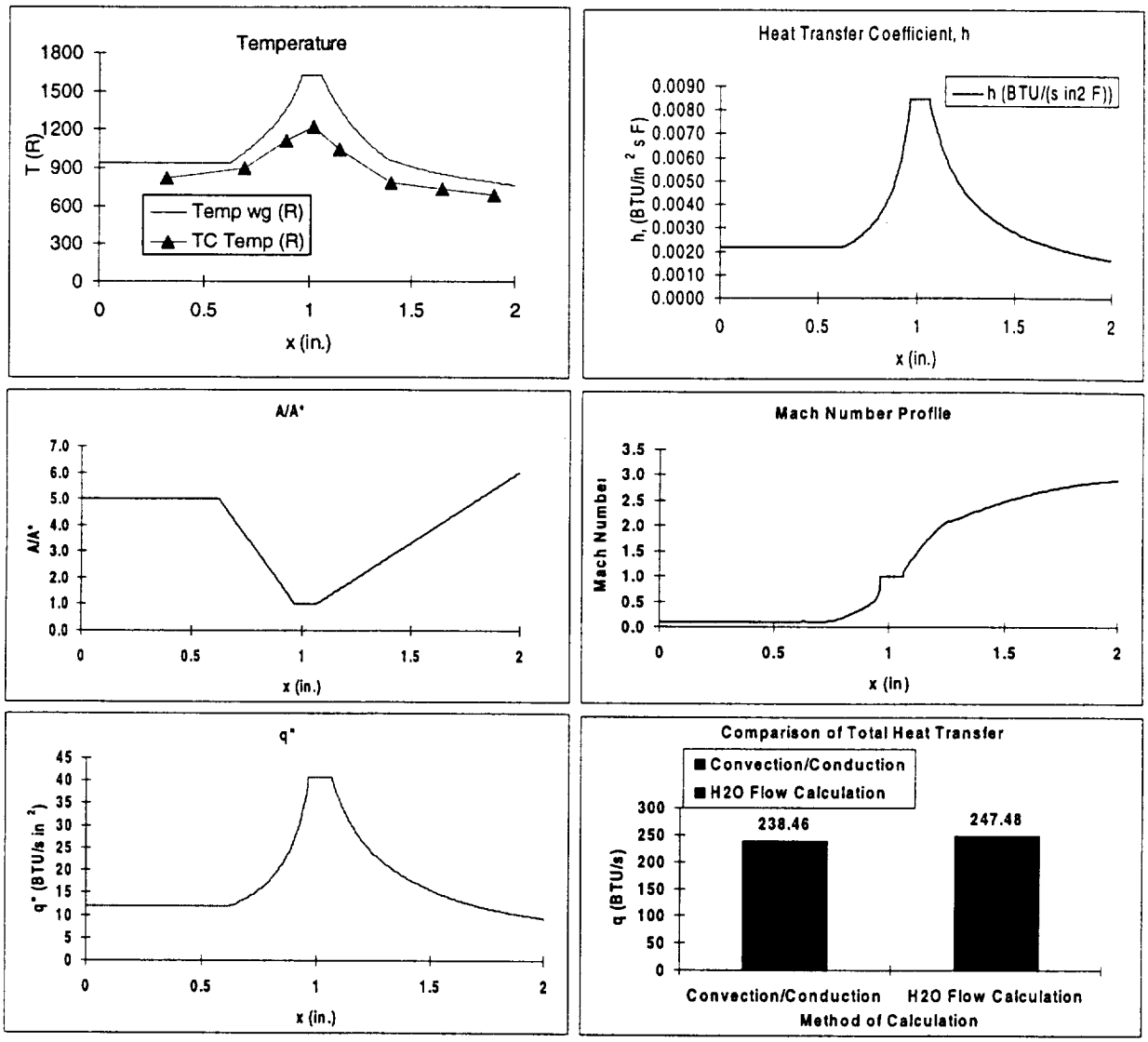


**Fig. 8. One-dimensional analysis for O/F=8, $P_c$=500 psia case.**

## VI References


[1] Bartz, D. R., "An Approximate Form of Compressible Turbulent Boundary Layer Development in Convergent-divergent Nozzles," Trans. ASME 77, 1955, pp.1235-1245.

[2] McBride, B. J. and Gordon, S., Computer Program for Calculation of Complex Chemical Equilibrium Compositions and Applications, NASA Reference Publication 1311, 1996.

# APPENDIX

Proceedings of the
33rd ASME/AIChE/ANS/AIAA National Heat Transfer Conference
August 15-17, 1999, Albuquerque, New Mexico

NHTC99-252

# EXPERIMENTAL STUDIES OF HEAT TRANSFER IN RECTANGULAR NOZZLES FOR CFD DESIGN METHODOLOGY

**Sibtosh Pal[†], Kevin Tucker[‡], Matthew Lehman[†], Robert J. Santoro[†]**

[†]Propulsion Engineering Research Center
Department of Mechanical and Nuclear Engineering
The Pennsylvania State University
University Park, Pennsylvania 16802

[‡]Fluid Dynamics Analysis Branch
NASA Marshall Space Flight Center
Huntsville, AL 35812

## ABSTRACT

Rocket thrusters for Rocket Based Combined Cycle (RBCC) engines typically operate with hydrogen/oxygen propellants in a very compact space. Chamber diameters are on the order of 10-15 mm and throat diameters are as small as 2.5 mm. Packaging considerations lead to designs with either axisymmetric or two-dimensional throat sections. Nozzles tend to be either two- or three-dimensional. Heat transfer characteristics, particularly in the throat, where the peak heat flux occurs, are not well understood. Heat transfer predictions for these small thrusters have been made with one-dimensional analysis such as the Bartz equation or scaling of test data from much larger thrusters. The current work attempts to fill this void through a combined experimental/analytical program that examines the heat transfer characteristics of a gaseous oxygen ($GO_2$)/gaseous hydrogen ($GH_2$) two-dimensional compact rocket thruster. The experiments involved measuring the axial wall temperature profile in the nozzle region of a water-cooled gaseous oxygen/gaseous hydrogen rocket thruster at a pressure of 3.45 MPa. The wall temperature measurements in the thruster nozzle in concert with Bartz's correlation are utilized in a one-dimensional model to obtain axial profiles of nozzle wall heat flux. A computational Fluid Dynamics (CFD) model is also used to independently predict the nozzle wall heat flux. The results of both analyses are integrated to obtain the overall heat transfer and are compared to measurements of the bulk heat transfer to the cooling water. The results show good agreement and indicate that both Bartz's correlation and CFD methodologies can be confidently used for estimating heat transfer in two-dimensional compact rocket thrusters.

## NOMENCLATURE

| | |
|---|---|
| $A$ | area |
| $A^*$ | area at nozzle throat |
| $c^*$ | characteristic velocity |
| $C_1, C_2, C_\mu$ | turbulence modeling constants |
| $C_p$ | specific heat |
| $D^*$ | throat diameter, taken here as hydraulic diameter |
| $G$ | geometry matrices |
| $h$ | convective heat transfer coefficient |
| $H$ | total enthalpy |
| $J$ | Jacobian of coordinate transformation |
| $k$ | thermal conductivity or turbulent kinetic energy |
| $M$ | local Mach number |
| $N$ | total number of chemical species |
| O/F | oxidizer to fuel mass flowrate ratio |
| $P$ | pressure |
| $Pr$ | Prandtl number |
| $q$ | $l,u,v,H,k,\varepsilon$ or $\rho_i$ or heat flow rate |
| $q''$ | heat flux |
| $r_c$ | throat radius of curvature (taken as 2.54 mm) |
| $S_q$ | source term for equation $q$ |
| $T$ | temperature |
| $T^+$ | non-dimensional temperature |
| $t$ | time |
| $U$ | volume-weighted contravariant velocity |
| $u, v$ | mean velocities in two directions |
| $u_\tau$ | wall friction velocity |
| $u^+$ | non-dimensional velocity, $(u/u_\tau)$ |
| $x$ | axial distance |
| $\Delta y$ | normal distance from wall to thermocouple location |

| | |
|---|---|
| $y^+$ | non-dimensional distance, $\left(y_p u_\tau \rho/\mu\right)$ |
| $\varepsilon$ | turbulent kinetic energy dissipation rate |
| $\gamma$ | ratio of specific heats |
| $\mu$ | dynamic viscosity or effective viscosity, $(\mu_l + \mu_t)$ |
| $\xi$ | computational coordinates |
| $\Pi$ | turbulent kinetic energy production |
| $\varpi$ | 0.6 for diatomic gases (assumed to be correct here) |
| $\rho$ | density |
| $\sigma_q$ | turbulence modeling constant |
| $\omega$ | chemical species production rate |

*Subscripts*

| | |
|---|---|
| $c$ | chamber |
| $g$ | hot gas side |
| $i$ | species |
| $l$ | laminar flow |
| 0 | stagnation conditions |
| $p$ | wall function point |
| $t$ | turbulent flow |
| $w$ | wall |

## INTRODUCTION

A steady interest in achieving low cost, reliable access to space drives constant efforts to develop advanced technologies for space transportation systems. A primary element of this goal lies in the development of advanced propulsion systems capable of meeting both performance and mission goals. The Rocket Based Combined Cycle (RBCC) is one promising approach that has received considerable interest throughout the last 30 years. The RBCC design utilizes air-breathing propulsion along with rocket propulsion to take advantage of the ambient oxidizer present in the lower atmosphere. Although there are various approaches being considered for the RBCC engine concept,[1] the cycle can be mainly divided into four regimes, viz. rocket-ejector, ramjet, scramjet and rocket-only. The engine can be designed to utilize simultaneous mixing and combustion (SMC) or diffusion and after burning (DAB) schemes.[2] The generic design consists of a variable area inlet section, duct section with multiple rockets, combustor section and nozzle section. Depending on the type of scheme employed, the rockets are operated either at stoichiometric conditions (DAB) or at fuel-rich conditions (SMC). The rockets act to induce air into the engine in the low Mach number (0 to approximately 2) range before transition to the ramjet mode. The rockets are again operated in the rocket-only mode with the engine inlet closed in the exo-atmosphere flight profile of the engine. The design of these highly integrated rocket thrusters and more specifically, the heat transfer characteristics in the nozzles of these engines constitutes the scope of the experimental and analytical efforts presented in this paper.

Rocket thrusters for RBCC applications are typically compact and in some instances 'two-dimensional" in geometry. Chamber dimensions are on the order of 10-15 mm and throat diameters as small as 2.5 mm. Packaging considerations lead to designs with either axisymmetric or two-dimensional throat sections. Nozzles tend to be either two or three-dimensional. Although various propellant combinations can in theory be utilized for powering these rockets, $GO_2/GH_2$ is the propellant combination of choice. The design pressures for these small thrusters can be as much as 7 MPa for total propellant flowrates of 0.5 kg/s. Since the environment in the thruster can be extremely harsh due to stoichiometric operation, the design of the thruster requires proven predictive capabilities such that proper cooling schemes can be implemented. The current analysis approach is to utilize the Bartz correlation[3] to predict the thruster heat transfer characteristics. The Bartz correlation has been proven to be robust for rocket design, however, the correlation has not been verified for small compact combustors.

The current work reports on experiments and both one-dimensional and computational fluid dynamics (CFD) analyses conducted to understand the nozzle heat transfer characteristics of rectangular cross-sectioned compact $GO_2/GH_2$ thrusters. The experiments involved using a highly instrumented thruster specifically designed for testing the ejector mode of a sector RBCC rig.[4] The experimental heat transfer results are compared with predictions using Bartz's correlation and CFD modeling results.

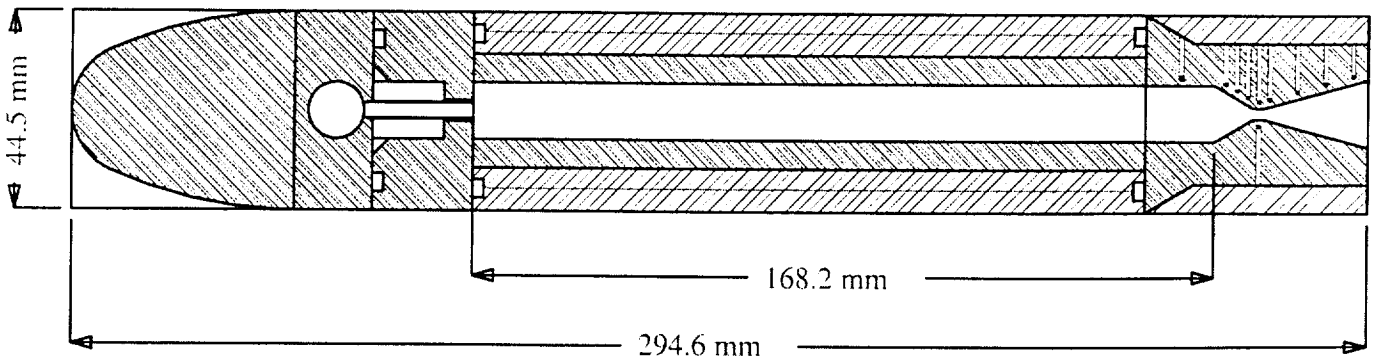


**Fig. 1. Schematic of the rocket thruster. The injector has six shear coaxial injector elements arranged linearly. The chamber is 168.2 mm long with a width and height of 76.2 mm and 12.7 mm, respectively. The nozzle throat width and height dimensions are 76.2 mm and 2.54 mm, respectively for a width to height ratio of 30.**

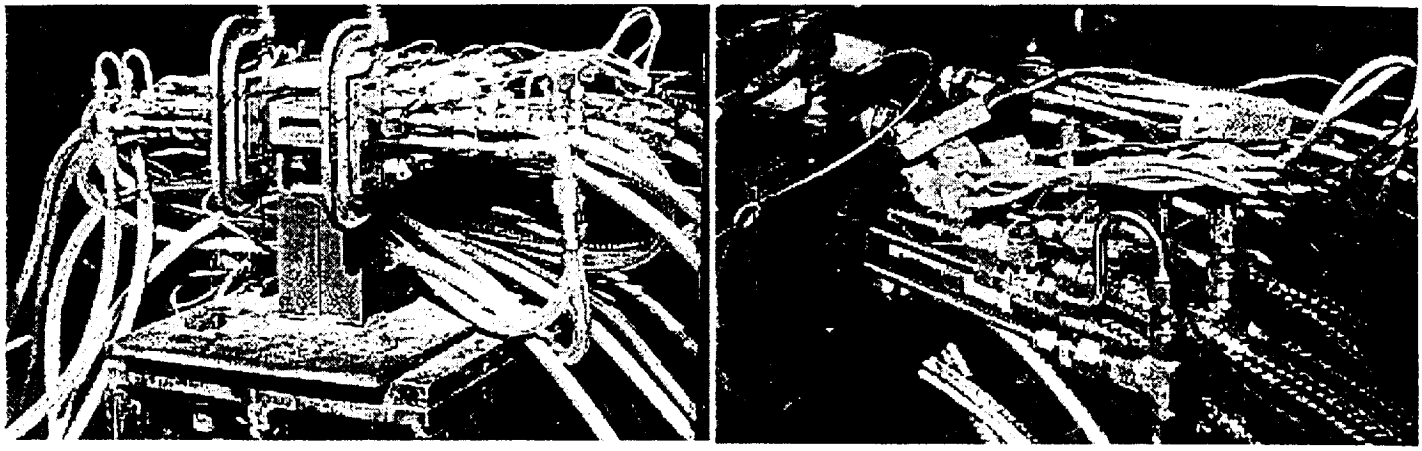

**Fig. 2. Photographs of rocket assembly. Photograph on left shows nozzle exit plane, whereas photograph on right shows a side view of the assembly including the individual thermocouple leads. The thermocouple wires, propellant feed lines, and water coolant lines are also seen.**

## EXPERIMENTAL

The heat transfer experiments were performed at the Cryogenic Combustion Laboratory at Penn State utilizing a multi-section rocket thruster. An assembly schematic is shown in Fig. 1, whereas two photographs of the complete hardware are shown in Fig. 2. The experimental setup includes an injector section, a chamber section, and a thermocouple-instrumented nozzle section. The injector body includes a linear array of six oxidizer-centered $GO_2/GH_2$ shear coaxial injector elements and is not actively cooled. The chamber section includes the pressure port, igniter mount, and a small viewing window to monitor ignition visually. Both the chamber and nozzle sections are actively cooled with water during the rocket firing. Nozzle design details are provided in the following subsection.

### Instrumented Rocket Nozzle

A schematic of the instrumented nozzle is shown in Fig. 3 with flow from left to right. The design includes two oxygen-free high-conductivity (OFHC) copper sections welded together to make up the nozzle flow path with stainless steel plates welded on top and bottom for strength purposes. The water passages, on all four sides of the nozzle, were individually drilled and closed off by welding. The Type-K thermocouples were silver-brazed to the bottom of their respective holes with approximately 1.27 mm of material separating them from the combustion gases. Thermocouples #1-#9 run along the top of the nozzle profile and #10 provides a second measurement at the throat from the bottom side. Contact was compromised for thermocouples #3 and #10 during the thermocouple mounting process and these two thermocouples were deemed unusable. The remaining eight thermocouples were used throughout the entire test sequence.

### Flow Conditions

Experiments were carried out for the target flow conditions summarized in Table 1. For the experiments, $GO_2/GH_2$ mixture ratios of 4, 6, and 8 and chamber pressures of 1.38, 2.07, 2.76, and 3.45 MPa were tested. Since the rocket hardware was not changed throughout the experiments, higher chamber pressures were achieved through increased propellant mass flow rates. For each flow condition, two 4 second duration rocket firings were made.

The cooling water flow system was split into two separate lines supplying the rocket chamber and nozzle sections. For each sub-system, the mass flow rate of water was calibrated for the upstream manifold pressure. The water flow rate to the nozzle was nominally 2.35 kg/s. For each firing, inlet manifold pressure as well as inlet and exit water temperature were recorded.

The analyses, both one-dimensional and CFD, were performed for test case 12 highlighted in Table 1 corresponding to the stoichiometric case at a chamber pressure of 3.45 MPa. This case was chosen for the analyses because the nozzle was designed to be perfectly expanded for these flow conditions.

**Table 1. Target Flow Conditions.**

| Case # | $GO_2$ Flowrate ($\times 10^{-3}$ kg/s) | $GH_2$ Flowrate ($\times 10^{-3}$ kg/s) | O/F | $P_c$ (MPa) |
|---|---|---|---|---|
| 1 | 85.3 | 21.3 | 4 | 1.38 |
| 2 | 98.5 | 16.4 | 6 | 1.38 |
| 3 | 110.3 | 13.8 | 8 | 1.38 |
| 4 | 127.9 | 32.0 | 4 | 2.07 |
| 5 | 147.7 | 24.6 | 6 | 2.07 |
| 6 | 165.5 | 20.7 | 8 | 2.07 |
| 7 | 170.5 | 42.6 | 4 | 2.76 |
| 8 | 196.9 | 32.8 | 6 | 2.76 |
| 9 | 220.7 | 27.6 | 8 | 2.76 |
| 10 | 213.2 | 53.3 | 4 | 3.45 |
| 11 | 246.2 | 41.0 | 6 | 3.45 |
| ***12*** | ***275.9*** | ***34.5*** | ***8*** | ***3.45*** |

## ANALYSES PROCEDURE

Two levels of analyses were conducted in support of the experiments. The first analysis used a one-dimensional model based on Bartz's correlation. The second analysis procedure involved a two-dimensional CFD calculation of the chamber/nozzle flowfield to predict the nozzle heat transfer characteristics. These two analytical procedures are briefly described next.

### One-Dimensional Model

The one-dimensional analysis used for evaluating the experimental measurements is presented here. The one-dimensional assumption asserts that at any axial location within the nozzle, all temperatures are constant. While this assumption may not be truly accurate, deviation from one-dimensionality can not be accounted for with the current measurements.

The analysis presented here is based on simple energy balance. Under steady state conditions, the bulk energy increase in the cooling water is equal to the heat transferred to the nozzle wall from the hot gases. There is no ambiguity in the measurement of the change in temperature of the cooling fluid. The total heat transferred from the hot gas to the chamber wall is calculated by integrating along the nozzle flow path. For the integration, Bartz's correlation[3] is used for obtaining the convective heat transfer coefficient.

$$h = \left[\frac{0.026}{(D^*)^{0.2}}\left(\frac{\mu^{0.2}}{Pr^{0.6}}C_p\right)_o\left(\frac{P_o}{c^*}\right)^{0.8}\left(\frac{D^*}{r_c}\right)^{0.1}\right]\left(\frac{A^*}{A}\right)^{0.9}\sigma \qquad \text{.....(1)}$$

where

$$\sigma = \frac{1}{\left[\frac{1}{2}\frac{T_{wg}}{T_{og}}\left(1+\frac{\gamma-1}{2}M^2\right)+\frac{1}{2}\right]^{0.8-0.2\varpi}\left(1+\frac{\gamma-1}{2}M^2\right)^{0.2\varpi}} \qquad \text{.....(2)}$$

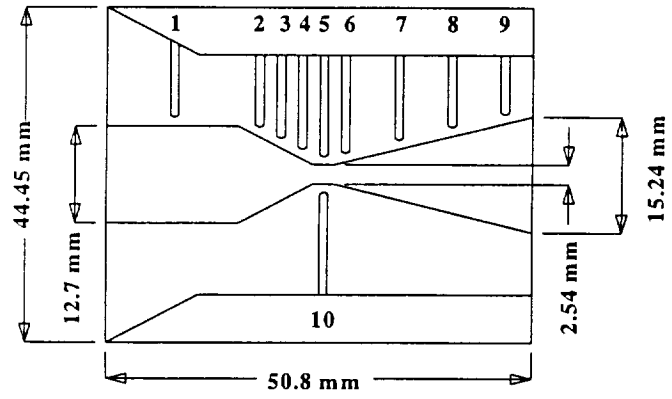


**Fig. 3. Schematic of the instrumented rocket nozzle section. From the nozzle inlet plane, the thermocouples are located at 8.1, 18.3, 20.8, 23.4, 25.9, 28.4, 34.8, 41.1, and 47.5 mm.**

For Eq. 1, the quantity in the square brackets is a constant throughout the converging-diverging section of the nozzle.

Since the nozzle thermocouples measure the metal temperature 1.27 mm from the hot wall surface, the following equation was used to calculate the temperature at the hot wall surface:

$$-k\frac{T_{thermocouple}-T_{wg}}{\Delta y} = h\left(T_{og}-T_{wg}\right) \qquad (3)$$

The use of this equation is based on the assumption that conduction occurs only normal to the boundaries, i.e. axial conduction in the metal is not considered. The above three coupled equations were numerically integrated to obtain the nozzle heat transfer characteristics.

### CFD Model

The FDNS CFD code[5] was used in the current work to model the hot gas-side flow field. FDNS has been in use at MSFC for several years and has been validated for, and successfully applied to, a broad range of combustion problems. Examples of relevant applications include flowfield analyses for rocket injectors,[6,7] preburners,[8,9] main combustion chambers,[6] nozzles[11,12] and plumes.[11-15]

The overall code algorithm along with details of the current set of calculations is presented next.

### FDNS Code

FDNS solves the equations which govern the turbulent, chemically reacting flow for this and similar problems. These non-linear, coupled equations include the Navier-Stokes equations, energy equation, two-equation turbulence models, and chemical species continuity equations. In general curvilinear coordinates, the Reynolds-averaged transport equations can be represented by

$$\left(\frac{1}{J}\right)\left(\frac{\partial pq}{\partial t}\right) = \frac{\partial\left[-pUq+\left(\mu/\sigma_q\right)G\left(\partial q/\partial\xi\right)\right]}{\partial\xi}+\frac{S_q}{J} \qquad (4)$$

where $q$ represents $1, u, v, H, k, \varepsilon$ and $\rho_i$, respectively. These represent the equations of continuity, x- and y- momentum, enthalpy, turbulent kinetic energy, turbulent kinetic energy dissipation rate, and density fractions. When the turbulent eddy viscosity concept is used, the effective eddy viscosity is given by $\mu$. The turbulent eddy viscosity is given by $\mu_t = \rho C_\mu k^2/\varepsilon$, where $C_\mu$ is a turbulence modeling constant. Values for the turbulence modeling constant, $\sigma_q$, and relations for the source terms, $S_q$, are given in Table 2. The ideal gas law is used as the equation of state. A nine reaction, six species finite rate reaction set is used to model the $O_2/H_2$ chemistry. The reactions are shown in Table 3.

Several two-equation turbulence models are available for use in FDNS; high and low Reynolds number models and models with extensions and corrections for compressibility.[16]

**Table 2. $\sigma_q$ and $S_q$ for the transport equations**

| $q$ | $\sigma_q$ | $S_q$ |
|---|---|---|
| 1 | 1.00 | 0 |
| $u$ | 1.00 | $-P_x + \nabla\left[\mu\left(u_j\right)_x\right] - (2/3)\left(\mu\nabla u_j\right)_x$ |
| $v$ | 1.00 | $-P_y + \nabla\left[\mu\left(u_j\right)_y\right] - (2/3)\left(\mu\nabla u_j\right)_y$ |
| $H$ | 0.95 | $DP/DT + \phi$ |
| $k$ | 1.00 | $\rho(\Pi - \varepsilon)$ |
| $\varepsilon$ | 1.30 | $\rho(\varepsilon/k)\left(C_1\Pi - C_2\varepsilon\right)$ |
| $\rho_i$ | 1.00 | $\omega_i, i = 1, 2, \ldots, N$ |

**Table 3. Reactions**

$$H_2 + O_2 \rightarrow 2OH$$
$$H_2 + OH \rightarrow H_2O + H$$
$$2OH \rightarrow H_2O + O$$
$$H_2 + O \rightarrow H + OH$$
$$O_2 + H \rightarrow O + OH$$
$$H + O \rightarrow OH$$
$$2O \rightarrow O_2$$
$$2H \rightarrow H_2$$
$$H + OH \rightarrow H_2O$$

The model employed in this study is the original Jones and Launder $k-\varepsilon$ model.[17] The source terms for the transport equations for this model are noted in Table 2. The constants $C_1$ and $C_2$ correspond to their original values of 1.43 and 1.92, respectively.

A pressure-based predictor/multi-corrector solution procedure is employed in FDNS.[18] The basic notion is to correct the pressure and velocity fields, based on the continuity equation, thereby enforcing velocity coupling. This pressure based method is suitable for all speed flow calculations.

Finite difference approximations are employed to discretize the transport equations onto structured grid systems.[16] Second-order upwind, third order upwind, or central differencing schemes plus adaptive second-order and fourth-order dissipation terms are used to approximate the convective terms in the transport equations. To ensure positive results for some scalar quantities such as turbulent kinetic energy and specie mass fractions, a first order upwind scheme is employed in these equations.

When a high-Reynolds number turbulence model is chosen, FDNS uses a modified wall function approach to obtain near wall resolution of the velocity field. This approach incorporates a universal velocity profile[19] given by

$$u^+ = ln\left[\left(y^+ + 11\right)^{4.02} \Big/ \left(y^{+2} - 7.36y^+ + 83.3\right)^{0.79}\right] + 5.63\tan^{-1}\left(0.12y^+ - 0.441\right) - 3.81 \quad (5)$$

and a universal temperature profile[20] given by

$$T^+ = u^+ 12.8\left(Pr_l^{0.68} - 1\right) \quad (6)$$

## Thruster Model

The thruster grid shown in the first inset graph of Fig. 4 is two-dimensional and has 131 nodes in the axial direction and 41 nodes in the radial direction. Note that only the part of the grid corresponding to the nozzle section of the thruster is shown. Also, for visual clarity, alternate j-lines have been deleted in the figure. The grid represents half of a slice of the thruster taken along an axial plane. Since the axial plane is symmetrical about the centerline, the calculation domain consists of only half of this plane. The grid shown in Fig. 4 (a) has been rotated about the symmetry plane for visual clarity. The grid was generated using the GRIDGEN software package.[21]

The inlet flow boundary was modeled with the mass flowrate fixed at the level specified by the experiment. Details of the injector elements were not modeled. The fuel and oxidizer were assumed to be completely mixed. Equilibrium properties to specify the inlet were obtained using CEA[22] at the experimental chamber pressure and mixture ratio. The downstream boundary was treated as an outlet where all the variables are extrapolated in the direction of the flow. An adaptive gradient detection extrapolation, where the order of extrapolation depends on the gradient strength, is employed for velocity vectors and pressure and temperature fields to provide smooth wave propagation through the outlet boundary. The symmetry boundary treatment is such that normal velocity vector components are assigned to zero so that resultant vectors are tangent to the symmetry plane. The thruster wall was treated with a no-slip condition. The thermal boundary condition at the wall was a fixed temperature distribution along the wall.

An iterative solution procedure was employed since the experimentally-determined temperature boundary condition is located not on the thruster hot gas wall, but inside the wall. The wall temperatures from the Bartz analysis were interpolated on the grid wall for an initial estimate. The CFD model was run to convergence with the convective heat flux from the hot gas to the wall calculated based on the presumed wall temperatures. Using energy conservation, this heat flux was then applied as the heat flux in the copper thruster wall that required calculation of a new hot gas wall temperature using Eq. (3). This temperature was then interpolated back onto the grid and the solution carried on in this iterative fashion until the convective and conductive heat fluxes were balanced.

## RESULTS AND DISCUSSION

The results presented here are confined to the flow conditions corresponding to Case 12 in Table 1. As mentioned earlier, this particular case was chosen for analyes because the flowfield in the nozzle divergence section is perfectly expanded. The CFD predictions of the flowfield in the nozzle

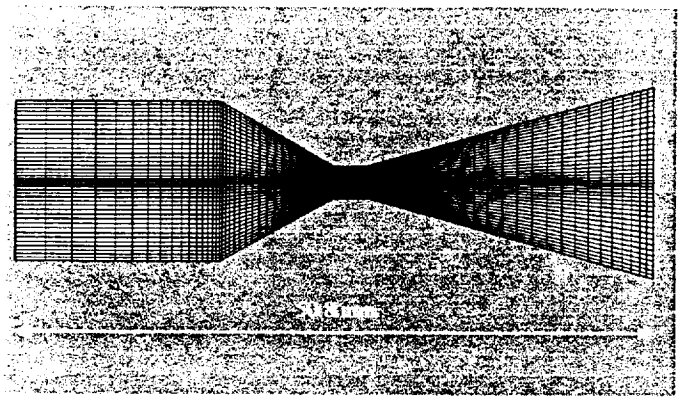

(a) Grid used for CFD calculations in nozzle section. (every other j-line has been removed for clarity)

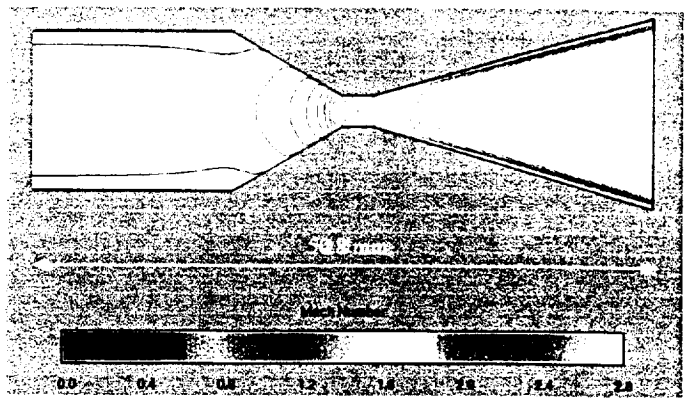

(b) Mach number contours in nozzle section.

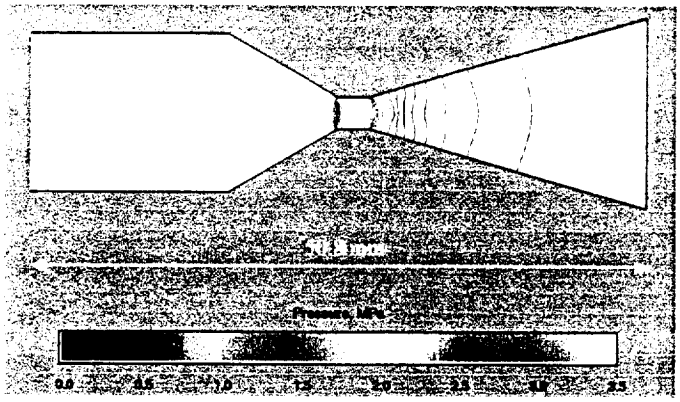

(c) Pressure contours in nozzle section.

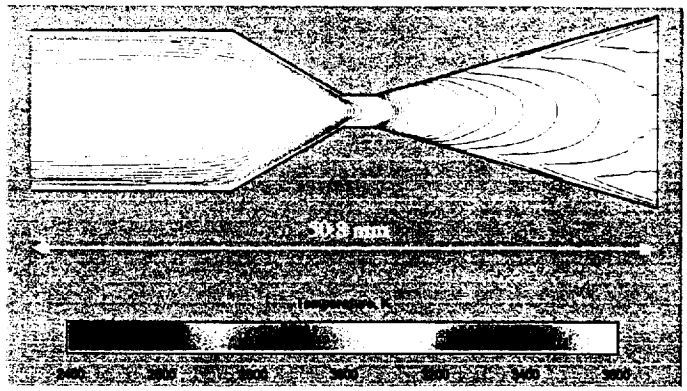

(d) Temperature contours in nozzle section.

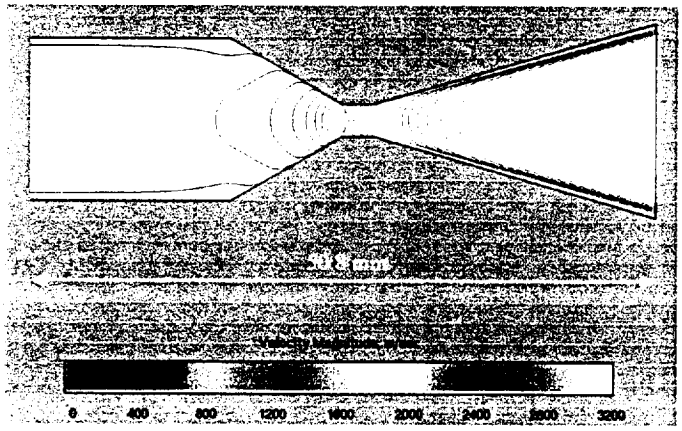

(e) Velocity magnitude in nozzle section.

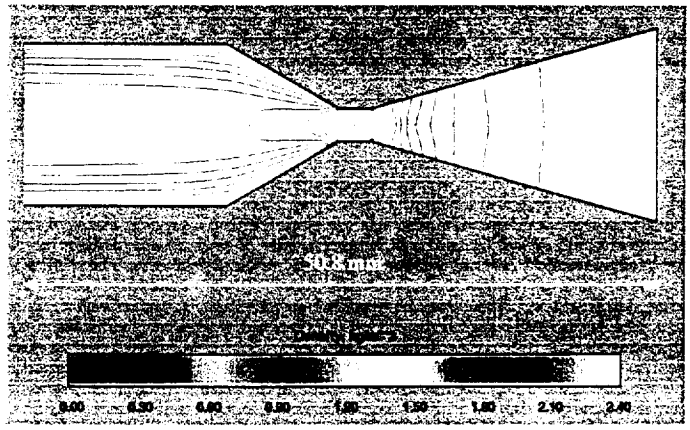

(f) Density contours in nozzle section.

**Fig. 4. CFD model predictions for rocket nozzle. Hydrogen/oxygen combustion at O/F=8. Chamber pressure of 3.45 MPa.**

for this case are described first followed by the nozzle heat transfer characteristics.

## Nozzle Flowfield Description

The CFD calculations were conducted for the entire flowfield, i.e. both the chamber and nozzle sections. The results shown here are for only the nozzle section. The grid used for the calculations along with contour plots of the Mach number, pressure, temperature, axial velocity magnitude and density are shown in the inset graphs of Fig. 4. As noted earlier, for the calculations, combustion is assumed to be complete at the injector face. The flow conditions of the experiment in concert with CEA[22] predictions of the properties are used to specify the inlet boundary conditions. The properties obtained from CEA are summarized in Table 4.

**Table 4. CEA Results for Properties.**

| | |
|---|---|
| Chamber Pressure (MPa) | 3.45 |
| $GO_2$ Flowrate ($\times 10^{-3}$ kg/s) | 275.9 |
| $GH_2$ Flowrate ($\times 10^{-3}$ kg/s) | 34.5 |
| Nozzle throat area ($mm^2$) | 193.55 |
| Temperature (K) | 3575.7 |
| Molecular Weight | 15.68 |
| Cp (kJ/kg•K) | 3.228 |
| $\gamma$ | 1.196 |
| Pr | 0.721 |
| $\mu$ (mP) | 1.117 |

The CFD flowfield results shown in Fig. 4 indicate that the flow is well behaved. Even though the nozzle geometry has three sharp corners, the flowfield does not have any corner recirculation zones. The Mach number contour plot indicates that the flow is choked in the upstream region of the nozzle throat. At the nozzle exit plane, the centerline values of Mach number pressure and temperature are 2.7, 0.111 MPa and 2590 K, respectively. These numbers indicate that the flowfield is near perfectly expanded. The temperature contour plot shows that at the beginning of the nozzle convergence section, the thermal boundary layer is thick. Inspection of the actual values shows that the temperature drops about 600 K from the core region to the wall at this axial point. Note that this is due to thermal boundary layer growth from the injector face plate (this part of solution is not shown in Fig. 4.)

## Nozzle Heat Transfer Characteristics

The nozzle heat transfer characteristics are obtained from the axial array of nozzle thermocouple temperature time trace measurements and the bulk temperature increase of the cooling water. For each test firing, rocket flow parameters were recorded to verify target conditions specified in Table 1. Nozzle themocouple as well as cooling water inlet and outlet temperatures were recorded at 200 Hz for a total of 10 seconds

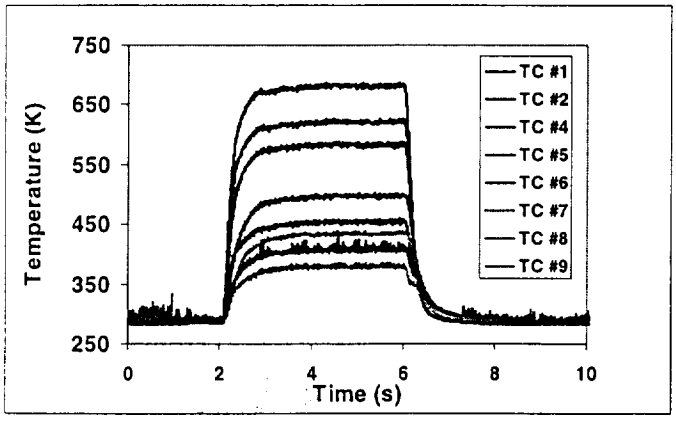


**Fig. 5. Temperature versus time for rocket nozzle. Hydrogen/oxygen combustion at O/F=8. Chamber pressure of 3.45 MPa. Note that all thermocouples achieve steadv state within 1.0 s.**

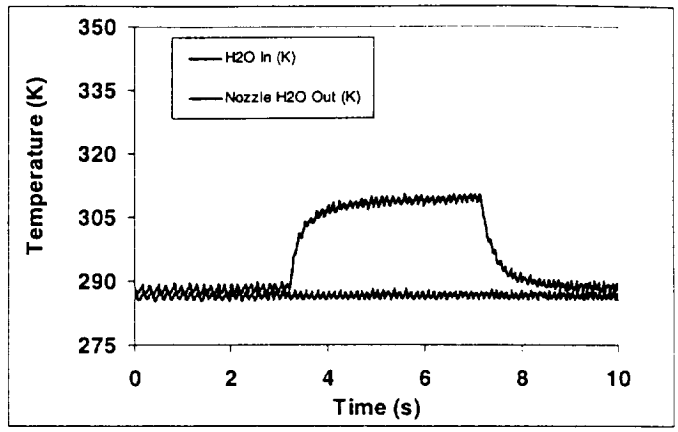


**Fig. 6. Inlet and outlet water flow temperature versus time for rocket nozzle. Hydrogen/oxygen combustion at O/F=8. Chamber pressure of 3.45 MPa.**

which included time before, during, and after the firing sequence. All averaged results were obtained from the final 1.5 seconds of steady state combustion for each firing.

The temperature versus time plots for the eight thermocouples are presented in Fig. 5 for Case #12, Table 1 corresponding to the O/F=8, chamber pressure of 3.45 MPa case. From Fig. 5, it is clear that the thermocouples reached their steady state temperatures well within the first second of the firing duration. The corresponding measured inlet and outlet water temperatures are plotted versus time in Fig. 6. These bulk water temperatures were used with the calibrated water flow rate values to calculate the bulk heat transfer from the nozzle to the water.

The one-dimensional analysis was conducted by numerically integrating the three coupled equations, Eqs. 1-3, discussed earlier to obtain the heat transfer for the test case. Properties were obtained using CEA[22]and are summarized in Table 4. For the integration, the nozzle was divided into four sections, viz. straight section, converging section, throat section, and the diverging section. For the constant area sections, constancy was assumed. The heat flux to the wall was also calculated from the CFD calculations. The key results of these analyses are plotted in Fig. 7.

The five axial profiles in Fig. 7 show the variation of area ratio, $A/A^*$, Mach number, wall temperature, heat transfer coefficient and heat flux with axial distance. The first parameter, $A/A^*$, simply indicates the nozzle geometry. The axial variation of Mach number is calculated using $A/A^*$ and the ratio of specific heats, $\gamma$, using isentropic relationships. The axial variation of temperature plot shows the actual thermocouple temperature measurements as well as the hot gas wall temperature calculated for both the one-dimensional and CFD analyses using Eq. 3. The two analysis procedures show hot gas wall wall temperatures that are nearly identical. The heat transfer coefficient as a function of axial distance is calculated using Eqs. 1-3 for only the one-dimensional analysis.

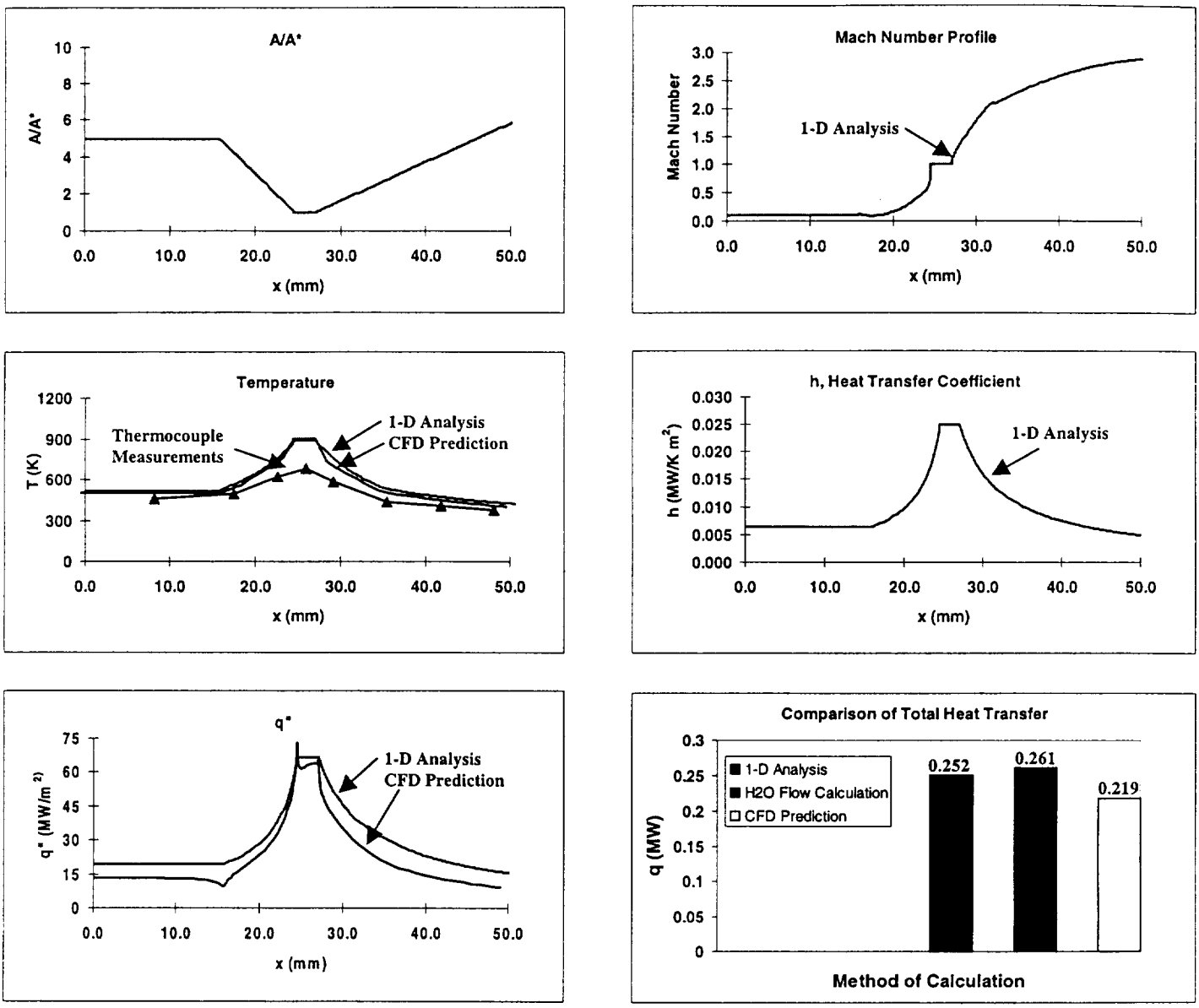


**Fig. 7. Results of one-dimensional and CFD analyses. Hydrogen/oxygen combustion at O/F=8. Chamber pressure of 3.45 MPa.**

The last axial profile shows the heat flux for both the one-dimensional and CFD analyses. The results show higher heat flux for the one-dimensional analysis than the CFD analysis in the straight, converging and diverging sections of the nozzle. However, in the nozzle throat region, the two analyses indicate almost identical heat flux levels. The two spikes evident in the CFD prediction at the beginning and end of the constant area throat region are due to increased levels of turbulent kinetic energy at the sharp corners.

The final step in the analytical procedures was to integrate the heat flux axially to obtain the overall nozzle heat flow rate. The results of this endeavor are shown in the last inset graph of Fig. 7. The integrated heat flow rate calculated from the one-dimensional analysis agrees to within 5% of the bulk energy increase of the coolant water flow, whereas agreement for the CFD prediction is within 15%. However, of more importance than the overall integrated comparison is the close agreement of the heat flux levels in the nozzle throat region between the one-dimensional analysis and CFD predictions since for rocket thruster design this region is the most sensitive.

These results indicate that both the Bartz's correlation and CFD can be applied confidently to predict heat flux levels for compact nozzle geometries.

## SUMMARY AND FUTURE WORK

The agreement in energy balance to within 5% for the one-dimensional analysis with Bartz's correlation for the prediction of the heat transfer coefficient was encouraging in terms of

confidence in the use of Bartz's equation for small scale rectangular rocket thrusters with high aspect ratio throats. Additionally, the good agreement, especially in the throat region, between the one-dimensional model prediction and the two-dimensional CFD prediction indicates that CFD has reached maturity to be used as a tool for rocket thruster design.

Future work will concentrate on additional CFD efforts. The effect of the thermal boundary layer thickness at the beginning of the nozzle convergence section on the throat heat flux will be systematically studied by performing calculations where the chamber length is progressively decreased. In additional, three-dimensional calculations will be undertaken to provide insight on the importance of nozzle throat corner effects.

## ACKNOWLEDGMENTS

The authors from Penn State acknowledge funding from NASA Marshall Space Flight Center under purchase order H-29688D. The authors also acknowledge Mr. L. Schaaf for his help in conducting the experiments.

## REFERENCES

[1] Escher, W. J. D., ed., The Synerjet Engine: Airbreathing/Rocket Combined-Cycle propulsion for Tomorrow's Space Transports, Society of Automotive Engineers, Inc., 1997.

[2] Billig, F. S., "Advanced Propulsion Technology Program, SSTO Low Speed System Assessment Final Report," The Johns Hopkins University Applied Physics Laboratory, JHU/APL AL-95-A050, June 1995.

[3] Bartz, D. R., "Turbulent Boundary-Layer Heat Transfer from Rapidly Accelerating Flow of Rocket Combustion Gases and of Hot Air," Advances in Heat Transfer, Vol. 2, 1965.

[4] Pal, S., Lehman, M., Broda, J. C. and Santoro, R. J., "Rocket Ejector Studies for Application to RBCC Engines: An Integrated Experimental/CFD Approach," The Thirty-Fourth JANNAF Combustion Meeting, FL, 1997.

[5] Chen, Y. S., "Compressible and Incompressible Flow Computations With a Pressure Based Method," AIAA Paper 89-0286, AIAA 27th Aerospace Sciences Meeting, Reno, NV January, 1989.

[6] Kim, Y. M., Shang, H.-M., Chen, C.-P., and Wang, T.-S., "Prediction of Confined Swirling Spray-Combustion Flows," Numerical Heat Transfer, Part A, Vol. 25, 1994, pp. 1-19.

[7] Chen, Y.-S., Shang. H.-M., Liaw, P., Chen, C.-P., and Wang, T.-S., "A Unified Two-Phase Numerical Method for General Gas-Liquid Flow Applications," 1995 ASME Summer Meeting, GL-19, Hilton Head, SC, August, 1995

[8] Wang, T.-S., Chen, Y.-S., Farmer, R. C. , and Tucker, P. K., "Numerical Investigation of the Transient SSME Fuel Preburner Combustor Flowfield," AIAA 90-0646, AIAA 28th Aerospace Sciences Meeting, Reno, NV, January 8-11, 1990.

[9] Foust, M. J. and Tucker, P. K., "Development of a Numerical Model for the Space Shuttle Main Engine Fuel Preburner," AIAA 94-2755, 30th AIAA/ASME /SAE/ASEE Joint Propulsion Conference and Exhibit, July, 1994, Indianapolis, IN.

[10] Wang, T.-S., and Luong, V., "Hot Gas-Side Heat Transfer in Liquid Rocket Engine Combustors," Journal of Thermophysics and Heat Transfer, Vol. 8, No. 3, July-Sept., 1994, pp. 524-530.

[11] Wang, T.-S., "Numerical Study of the Transient Nozzle Flow Separation of Liquid Rocket Engines," Computational Fluid Dynamics Journal, Vol. 1, No. 3, October, 1992, pp. 319-328.

[12] Tucker, P. K., and Warsi, S. A., "Axisymmetric Computational Fluid Dynamics Analysis of a Film/Dump-Cooled Rocket Nozzle Plume," AIAA 93-2349, 29th AIAA/ASME/SAE/ASEE Joint Propulsion Conference, June 28-30, 1993, Monterey, CA.

[13] Wang, T.-S., "Numerical Analysis of Base Flowfield for a Four-Engine Clustered Nozzle Configuration," Journal of Propulsion and Power, Vol. 11, No. 5, September-October, 1995, pp. 1076-1078.

[14] Wang. T.-S., "Grid-Resolved Analysis of a Four-Engine Clustered Nozzle Configuration," Journal of Spacecraft and Rockets, Vol. 33, No. 1, January-February, 1996, pp. 22-29.

[15] Wang, T.-S., McConnaughey, P. K., Warsi, S. A., and Chen, Y.-S., "Computational Pollutant Environment Assessment from Propulsion System Testing," Journal of Spacecraft and Rockets, Vol. 33, No. 3, May-June, 1996, pp. 386-392.

[16] Tucker, P. K. and Shyy, W., "A Numerical Analysis of Supersonic Flow Over an Axisymmetric Afterbody," AIAA 93-2347, 29th AIAA/SAE/ASME/ASEE Joint Propulsion Conference, June 28-30, 1993, Monterey, CA.

[17] Jones, W. P. and Launder, B. E., "The Prediction of Laminarization with a Two-Equation Model of Turbulence," International Developments in Heat Transfer, Vol. 15, pp. 303-314, 1972.

[18] Wang, T. S., and Chen, Y. S., "Unified Navier-Stokes Flowfield and Performance Analysis of Liquid Rocket Engines," Journal of Propulsion and Power, Vol. 9, No. 5, 1993, pp. 678-685.

[19] Liakopolous, A., "Explicit Representation of the Complete Velocity Profile in a Turbulent Boundary Layer," AIAA Journal, Vol. 22, No. 6, 1984, pp. 844-846.

[20] White, F. M., Viscous Fluid Flow, McGraw-Hill, New York, 1974.

[21] Steinbrenner, J. P. and Chowner, J. R., The GRIDGEN Version 8 Multiple Block Grid Generation Software," MDA Engineering Report 92-01, Arlington, TX, 1992.

[22] McBride, B. J. and Gordon, S., Computer Program for Calculation of Complex Equilibrium Compositions and Applications, NASA Reference Publication 1311, 1996.